Observation of Topological Spin Textures in Ferrimagnetic $Mn_{2-x}Zn_xSb$

Yue Li[1,*] | Md Rafique Un Nabi[2] | Hyowon Park[1,3] | Yuzi Liu[4] | Stephan Rosenkranz[1] | Amanda K. Petford-Long[1,5] | Jin Hu[2,6] | Suzanne G.E. te Velthuis[1,*] | Charudatta Phatak[1,5,*]

[1]Materials Science Division, Argonne National Laboratory, Lemont, IL, 60439, USA

[2]Department of Physics, University of Arkansas, Fayetteville, AR, 72701, USA

[3]Department of Physics,University of Illinois Chicago,Chicago, IL, 60607,USA

[4]Center for Nanoscale Materials, Argonne National Laboratory, Lemont, IL, 60439, USA

[5]Department of Materials Science and Engineering, Northwestern University, Evanston, IL 60208, USA

[6]Materials Science and Engineering Program, University of Arkansas, Fayetteville, AR, 72701, USA

Correspondence
Yue Li, Charudatta Phatak, Suzanne G.E. te Velthuis
Email: yue.li@anl.gov, cd@anl.gov, tevelthuis@anl.gov

Ferrimagnets, which have both ferromagnetic and antiferromagnetic coupling are attracting increased attention in the realm of spintronic devices due to advantages such as ultrafast dynamics and a suppressed skyrmion Hall effect. Thus, understanding the behavior of non-trivial spin textures in ferrimagnets is crucial, however comprehensive reports on this topic remain limited. Here, we explore the magnetic spin textures of ferrimagnetic $Mn_{2-x}Zn_xSb$ (x = 0.85) as a function of temperature and applied magnetic field. Spin textures that can be tuned into a variety of states, including stripes, skyrmion bags, and a skyrmion lattice.Chiral Néel-type magnetic structures are visualized using Lorentz transmission electron microscopy. Mn(I) ions prefer shifting slightly toward to Sb sites, which may be due to a strong electrostatic interaction between Mn and Sb ions. The structure defect breaks the local structure symmetry and introduces the effective Dzyaloshinkii-Moriya interaction. Our work thus provides a pathway to use doping and heterogeneity in a ferrimagnet to control and generate chiral non-trivial spin textures.

KEYWORDS
Ferrimagnet, temperature dependence, Néel type, rich spin textures, Mn ion displacement, structural asymmetry

1 | INTRODUCTION

Magnetic skyrmions are topologically non-trivial spin textures that are fascinating not only due to their fundamental physics arising from symmetry breaking but also technologically useful for future spintronic applications[1–4]. The majority of the research on magnetic skyrmions has focused on ferromagnetic (FM) materials with broken symmetries either due to a chiral crystal lattice, such as MnSi[5], FeGe[6], Co-Mn-Zn,[7] or to asymmetric interfaces in heterostructures, for example in Ta/CoFeB/TaOx[8] or Pt/Co/X, where X is a heavy metal[9,10]. The interplay between the Heisenberg exchange and the anti-symmetric exchange, Dzyaloshinkii-Moriya interaction (DMI), leads to the formation of skyrmions of Bloch-type or Néel-type[11]. Bloch-type spin textures are stabilized due to inversion symmetry breaking of the bulk crystal, while the formation of Néel spin textures arises from the broken inversion symmetry at interfaces[12]. Recently, skyrmions have also been observed in achiral materials, which are stabilized due to long-range dipolar interactions. In particular, materials with achiral crystal lattices and competing types of magnetic order, such a ferrimagnetic (FiM) order, are extremely interesting as they provide additional degrees of freedom that can lead to a larger variety of topological spin textures and a rich phase space with respect to temperature and magnetic field[4]. Ferrimagnets have unbalanced antiparallel-aligned magnetic spins at inequivalent sublattices, simultaneously possessing antiferromagnetic (AFM) and ferromagnetic (FM) orders. This leads to unique magnetic properties: small stray field, small net magnetization and ultrafast dynamics[13,14]. Although bulk and interfacial DMI have been reported in FiM multilayers[15,16] and amorphous alloys[17], the DMI in FiM crystals still remain little known and has recently garnered interest.

One of the outstanding issues with skyrmions in FM materials is the skyrmion Hall effect, which results in a non-collinear motion of skyrmions with respect to an applied electric current[18,19]. This is not desirable for spintronic applications such as skyrmion racetrack mem-

ories. Here again, it has been predicted and observed that the use of FiM materials can lead to suppression of the skyrmion Hall effect due to competing magnetic order on different sublattices in the material[20,21]. The formation of skyrmions and chiral domains in FiM materials, due to the presence of a DMI has only recently been reported,[21–29] however, a majority of these material are based on rare-earth metals which are not earth-abundant and considered critical raw materials such as Gd, Tb, Dy as multilayers or alloys such as GdFeCo.

Mn_2Sb is a rare-earth-free FiM material that crystallized in a layered structure with a P4/nmm space group. It has two inequivalent Mn sites, Mn(I) and Mn(II), which have different magnetic moments and are coupled antiferromagnetically, leading to FiM order[30–32]. The difference in magnetisation of the two distinct Mn sublattices results in exotic temperature-dependent magnetic properties, such as the switching of the magnetic easy axis from the basal plane at low temperatures (<240 K) toward the *c* axis at higher temperatures (> 240 K)[30]. Doping the Mn_2Sb with transition metals such as Co[33,34], Cr[35] and Zn[32,36–39], can also be used to control the magnetic behavior. FiM $Mn_{2-x}Zn_xSb$, in which Zn atoms only substitute for the Mn(II) sites, displays rich temperature-dependent phase transitions and electronic properties as a function of the Zn content[32,36]: for example, when Zn atoms occupy all Mn(II) sites, MnZnSb becomes FM ordering at room temperature[37]. As a result, $Mn_{2-x}Zn_xSb$ offers a unique material platform to explore the effect of competing magnetic order (ferromagnetic and antiferromagnetic coupling) on emergence of non-trivial magnetic spin textures.

In this work, we explore the way in which temperature and applied field influence the formation of variety of topological spin textures in FiM $Mn_{2-x}Zn_xSb$ (x=0.85). We determine the type of spin texture and their behavior using a combination of magneto-optic Kerr effect (MOKE) microscopy and Lorentz transmission electron microscopy (LTEM). The observation of diverse spin textures (including the stripe structure, skyrmion lattice and skyrmion bag) in the bulk crystal is attributed to the variation of magnetic parameters, such as the uniaxial anisotropy, coercive field and saturation magnetization, as a function of temperature. The

chiral Néel-type domains were seen via the LTEM. The Mn atoms at the Mn(I) sites were found to be closer to the Sb atoms than the Mn(II) sites, determined using atomic-resolution scanning TEM (STEM) high-angle annular dark-field (HAADF) imaging. The displacement of Mn(I) sites could be responsible for breaking the inversion symmetry, thereby introducing the effective DMI to form the Néel-type spin textures.

2 | RESULTS AND DISCUSSION

2.1 | Temperature-dependent Magnetic properties

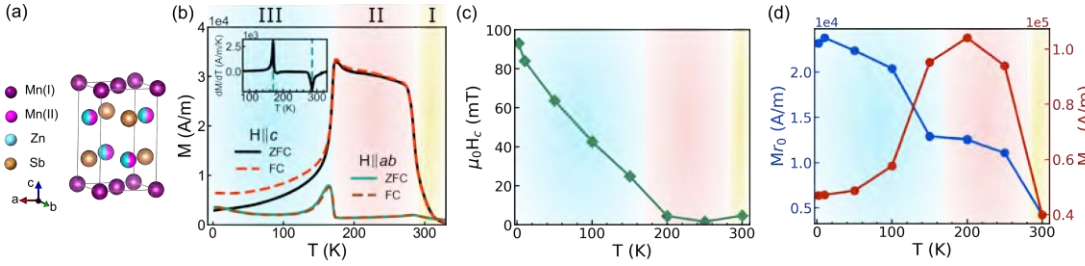

FIGURE 1 Temperature-dependent magnetic properties of a $Mn_{1.15}Zn_{0.85}Sb$ bulk crystal. (a) The schematic of crystal structure of $Mn_{2-x}Zn_xSb$[36]. (b) Magnetization as a function of temperature for zero-field-cooling (ZFC) and field-cooling (FC) protocols in a 50 mT magnetic field applied along the *c* axis or in the *ab* plane. The temperature-dependent curves can be divided into three temperature regimes, I, II and III. Inset is the derivative of the ZFC curve showing two phase transition temperatures at 170 K and 286 K. The background colors highlight the three temperature regimes. (c) Temperature-dependent coercive field, H_c, when the net magnetization is 0 A/m. (d) Temperature-dependence of the remnant magnetization M_{r0} (blue) and of the quasi-saturation magnetization M_{qs} (red) at a 400 mT applied magnetic field (red). The external magnetic field was applied along the *c* axis of crystal for (c) and (d).

In order to determine the magnetic behavior of $Mn_{1.15}Zn_{0.85}Sb$, we measured the temperature-dependent magnetization and hysteresis loops that determine the magnetic parameters, such as coercive field, remnant magnetization and perpendicular anisotropy, and the associated phase transitions. Figure 1(a) shows the out-of-plane ($H \parallel c$) and in-plane ($H \parallel ab$) magnetization as a function of temperature during the zero-field-cooling (ZFC) and field-cooling (FC)

protocols in a 50 mT magnetic field. The details of $Mn_{2-x}ZnxSb$ crystal orientation in our work is sketched in Figure 1(d)[36]. It can be seen that there are three regions showing different temperature-dependent magnetization behaviors across the temperature range from 2 K to 330 K, which are labeled as Regions I, II and III, with transition temperatures at 170 K and 286 K, as shown in the inset in Figure 1(a). The higher transition temperature corresponds to the transition from a paramagnetic state (Region I) to a FiM state (Region II). As the temperature is lowered, there is an gradual increase in magnetization along the *c*-axis (Region II) until approaching to 170 K, below which the magnetization along the *c*-axis decreases abruptly (Region III). In Region II, $Mn_{1.15}Zn_{0.85}Sb$ shows a strong perpendicular magnetic anisotropy, as measured from hysteresis loops (Supporting Figure S2), which decreases below 170 K (Region III) along with the decrease in magnetization. We also measured the magnetization in the *ab* plane which shows a slight increase near the lower transition temperature of 170 K. These measurements suggest that there could be a spin reorientation occurring near 170 K which tilts the magnetic moment of the Mn ions away from the *c*-axis and towards the *ab* plane[30,32,36]. The comparison of temperature-dependent magnetic magnetization under varying magnetic fields is detailed in Supporting Section S1.

Based on isothermal hysteresis measurements with the magnetic field along the *c* axis[36], we also determined the coercive field, and the remnant and quasi-saturation magnetization of $Mn_{1.15}Zn_{0.85}Sb$, which are also temperature dependent. The definitions of these three magnetic parameters are shown in Supporting Figure S2. Figure 1(b) shows that the value of the coercive field (H_c) is very low in the Regions I and II, and then increases as the temperature reduces into Region III. The temperature-dependent remnant magnetization (M_{r0}) (Figure 1(c)) slowly increases with decreasing temperature within each region but shows a significant change across the transition between regions. The increase in the remnant magnetization suggests a more square hysteresis loop (Supporting Figure S2). We also measured the magnetization at $\mu_0 H = 400$ mT applied along the *c* axis as a function of temperature (Fig-

ure 1(c)), which we refer as to the quasi-saturation magnetization (M_{qs}) since the upper and lower branch of the hysteresis loop almost overlap for all temperatures (see Supporting Figure S2). The behavior of this magnetic parameter shows a similar trend as the M vs. T curve for in Figure 1(a): the value of M_{qs} reaches a maximum value of 1.04×10^{-5} A/m in Region II and decreases as the temperature is reduced. These findings show that the FiM coupling in $Mn_{1.15}Zn_{0.85}Sb$ is strongly dependent on temperature, which results in the variation of the magnetic parameters of the bulk crystal.

2.2 | Diverse magnetic spin textures

To gain further insight into the effect of varying magnetic parameters on the spin textures, we systematically studied the temperature- and field-driven behavior in each of the three regimes. Polar MOKE microscopy was utilized to directly visualize real-space magnetic spin textures of a bulk $Mn_{1.15}Zn_{0.85}Sb$ crystal. The sample was cooled to a given temperature with the field applied perpendicular to the sample surface along the *c* axis and varied between 0 and 135 mT. Figure 2 shows the magnetic spin textures observed at specific applied field values and temperatures. At 300 K (region I), when the magnetization is very weak, we observe the formation of stripe domains in a low applied field as shown in Figure 2(a). Although the bulk crystal has paramagnetic order at a high temperature, 300 K is at the phase transition region, and magnetic net magnetic moment is not completely zero. As the applied field is increased (center and right panes of the figures), the stripe domains break down and initially form a mixed state of short stripes and skymionic bubbles at 67 mT, with a disorder skyrmion lattice forming at 87 mT magnetic field. All magnetic spin textures are polarized in an applied field of 97 mT. It should be noted that these skyrmionic bubbles are of the order of approximately 700 nm in diameter at the 87 mT magnetic field (see more details in Supporting Figure S3). We find that the skyrmions prefer forming at the intersection of a couple of stripe domains or at the

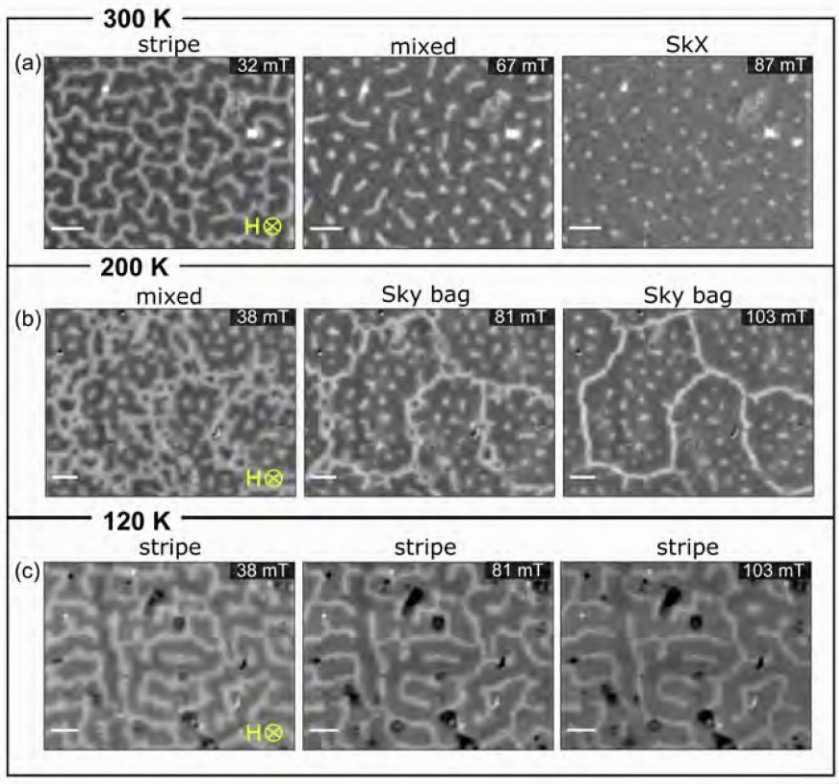

FIGURE 2 Magnetic spin textures observed at the surface of a bulk $Mn_{1.15}Zn_{0.85}Sb$ crystal. MOKE images showing evolution of the magnetic spin textures as a function of a magnetic field applied perpendicular to the sample and along the *c* axis, at temperatures of (a) 300 K (Region I), (b) 200 K (Region II) and (c) 120 K (Region III). SkX refers to a skyrmion lattice and 'Sky bag' to a skyrmion bag. Scale bars:5 μm for (a), 10 μm for (b) and (c).

end of stripe domains, and a few skrymions are created at the vicinity of structural defects (Supporting Video S1).

In region II at a temperature of 200 K, as discussed before, the perpendicular anisotropy and saturation magnetization are higher than those in region I, resulting in the formation of mixed states consisting of stripes and bubbles at a lower field ($\mu_0 H < 124$ mT), as shown in Figures 2(b) and Supporting Figure S4. As the field is increased to 81 mT, we observe an interesting transition of the spin texture to skyrmion lattices that are each enclosed in a large closed-loop stripe domain; these are referred to as skyrmion bags. The skyrmion bag configuration, which has a high topological charge, has been reported in a 2D liquid crystal[40] as well as in materi-

als with an intrinsic DMI, such as FeGe[41?]. Interestingly, unlike the isolated skyrmion bag in other published work, the connected skyrmion bags emerge in the $Mn_{1.15}Zn_{0.85}Sb$. As the field is increased up to 103 mT, the skyrmion bag configuration remains stable and the connected multiple domains shrink to a single looped stripe. The skyrmion bag configuration eventually breaks down to form a skyrmion lattice again at a field of 124 mT.

In the low-temperature regime (Region III) at 120 K, where the magnetization decreases significantly, we only observe the formation of stripe domains in an applied field range from 0 mT to 135 mT, as shown in Figure 2(c). The increase in the magnetic field results in narrowing the width of stripe domains. The sample was not fully saturated at the maximum applicable field in our experimental setup (135 mT). The formation of bubbles is not seen. This suggests that the out-of-plane anisotropy significantly reduces. The black spots in the images are surface contamination and could not be removed by image processing (details in the Methods section).

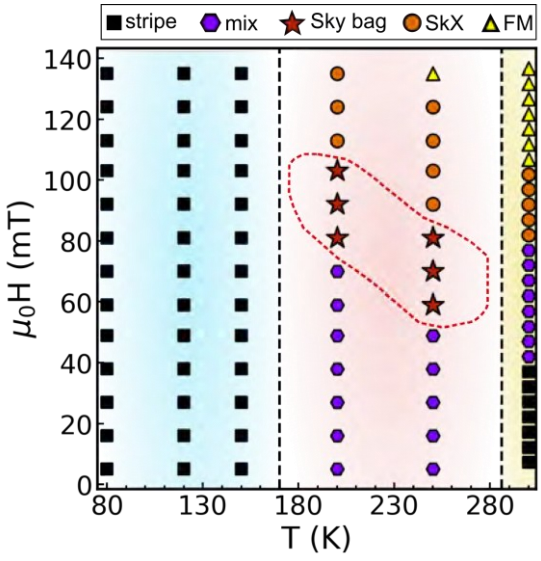

FIGURE 3 Magnetic phase diagram as a function of applied magnetic field at varying temperature, showing the formation of diverse spin textures, including stripe, mixed stripe and skyrmion, skyrmion (Sky) bag, skyrmion lattice (SkX) and FM states. The background colored gradients highlight the three temperature regimes, and the black dashed lines indicate the two phase transition temperatures (170 K and 286 K respectively). The red dashed curve marks the phase region where the Sky bag configuration is observed.

Based on our extensive imaging of the magnetic spin textures, we can establish a magnetic phase diagram for $Mn_{1.15}Zn_{0.85}Sb$ showing various spin textures that form as a function of temperature and magnetic field, as shown in Figure 3. The phase diagram explicitly demonstrates that the resulting magnetic spin texture is strongly associated with the three temperature regimes. In Region I, at higher temperature, the spin texture gradually evolves forming stripes, then a mixed state, then skyrmion lattices, and finally a uniformly-magnetized state as a function of applied field. However, as the perpendicular anisotropy increases, and thus the net magnetization along the c-axis, is dramatically enhanced in Region II. This leads to the formation of the skyrmion at a lower magnetic field, $\mu_0 H = 5$ mT (Supporting Figure S4) or $\mu_0 H = 0$ mT[42]. The zero-field skyrmions induced by the increase in the perpendicular anisotropy were also reported in the synthetic Pt/CoGd/Pt ferrimagnetic multilayers[43]. The similar mixed bubble and stripe domains, which introduced by the surface stay field, have been observed in a bulk cobalt crystal[44]. In addition, a unique skyrmion bag structure forms in the intermediate field range, along with a skyrmion lattice created at a higher magnetic field.

Finally in region III, due to a decrease in net magnetization along the c-axis, and a change in anisotropy, we only observe the formation of stripes across the entire applied field range. These findings show that the variation of FiM coupling as a function of temperature and applied field in $Mn_{1.15}Zn_{0.85}Sb$ can be leveraged to create a diverse variety of spin textures. It should be noted that the sample was cooled under a zero applied field to the specific temperature, at which the images were recorded, in all these cases,.

2.3 | In-situ temperature dependent imaging of Néel spin textures

To understand the nature of magnetic spin textures, we employed the LTEM for imaging of the magnetization distribution in $Mn_{1.15}Zn_{0.85}Sb$. The LTEM has the capability to efficiently determine whether the magnetic spin textures are Néel- or Bloch-type in a magnetic sample

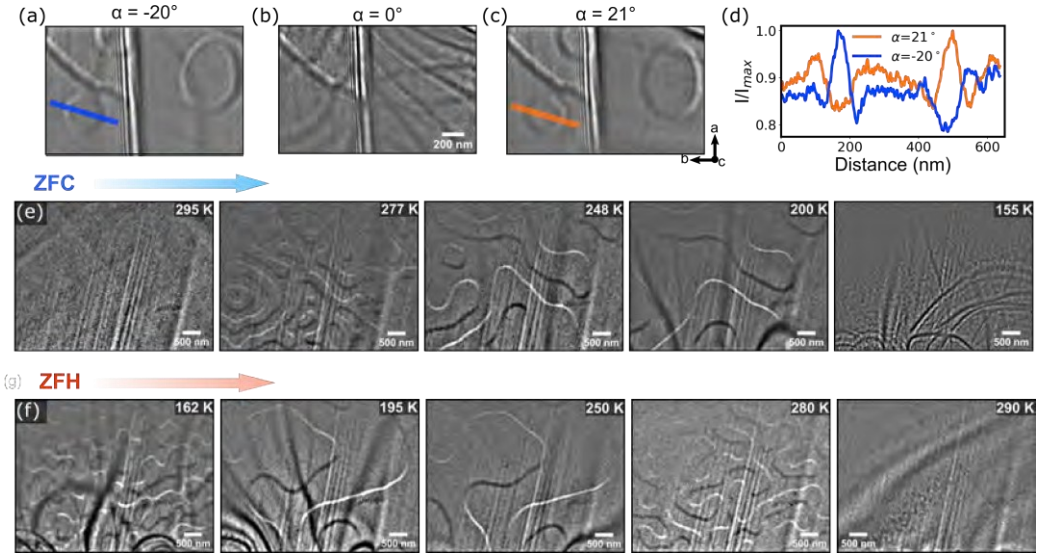

FIGURE 4 Evolution of Néel magnetic spin textures of a thin $Mn_{1.15}Zn_{0.85}Sb$ lamella, viewed along the [001] zone axis, as a function of temperature. (a−c) LTEM images recorded at 250 K of a thin lamella of $Mn_{1.15}Zn_{0.85}Sb$ as a function of tilt angle, α, showing the Néel-type magnetic spin texture. (d) Average intensity profile along the orange and the blue lines across the Néel-type skyrmions at tilt angles of $\alpha = -20^{\circ}$ and $\alpha = +21^{\circ}$. LTEM images of the evolution of a stripe spin texture as a function of temperature during (e) a ZFC run and (f) a ZFH run.

with strong perpendicular anisotropy, based on changes in image contrast as a function of sample tilt[45]. A thin TEM lamella (thickness < 200 nm) was prepared for LTEM imaging with a zone axis along [001] direction. Figures 1 (e-g) show out-of-focus LTEM images at varying tilt angles (-20°, 0° and 21°) at 250 K (temperature Region II). Skyrmions are visible in the images at non-zero tilt, but the magnetic contrast disappears when the sample is tilted to 0°, with the only contrast being due to bend contours . The projected in-plane magnetic induction from the two opposite tilt angles results in the domain contrast reversing as indicated by the blue and orange line plots shown in Figure 1 (h). The LTEM results indicate that the spin textures in $Mn_{1.15}Zn_{0.85}Sb$ are Néel-type, suggesting the presence of an Dzyaloshinkii-Moriya interaction (DMI) that results in the chiral domains. This agrees with previous work which has shown that $Mn_{1.15}Zn_{0.85}Sb$ exhibits a finite topological Hall effect[36]. This is quite surprising since the crystal structure of $Mn_{1.15}Zn_{0.85}Sb$ is tetragonal and centrosymmetric, belonging to

the *P4/nmm* space group.

However, it is worthy noting that the thicknesses of the LTEM lamella and MOKE bulk sample are different, the former being less than 200 nm and the latter being around 130 μm. The variation in the thickness can significantly alter the density, size and nature of spin textures[46–48]. It has been reported that the increase in the thickness would lead to the transformation from Néel to Bloch spin textures[49]. Rising thickness results in the increase of dipolar energy, which would favor the formation of Bloch domains[44,48]. Therefore, although the Néel spin texture is observed, the nature of spin texture in the bulk crystal could also be the Bloch type. Besides, the reduction of dimensionality of the lamella would introduce the boundary effect to impact the formation of spin texture. For example, the creation of stripe domains in the *ab* plane starts at the edge of the lamella (Supporting Figure S5).

In the previous section, we discussed the field-driven behavior of the spin textures in $Mn_{1.15}Zn_{0.85}Sb$ at a given fixed temperature in each of the three temperature regimes. It is also interesting to gain insight into how the spin textures evolve continuously as a function of temperature, and we can explore this at high spatial resolution using LTEM. We performed the in situ ZFC and zero field-heating (ZFH) experiments and recorded the LTEM images as displayed in Figure 4(a) and (b). The TEM lamella was fabricated along the *ab* plane, thereby resulting in the $c-$ axis and the easy axis of magnetization to aligned with the electron beam direction. During the ZFC experiment, at 295 K the magnetic contrast is not clearly evident, while the spin textures at 300 K in the MOKE experiment were clearly visible. This is most likely a result of sample thickness; the thickness of the LTEM sample is less than 200 nm, while the MOKE specimen was a bulk crystal with thickness of a few tens of microns. A similar scenario also occurs when the temperature is less than 155 K, as the magnetic moment is too weak in Region III to give rise to detectable LTEM contrast. A stripe spin texture is observed at 277 K, and as the temperature decreases, the width of the stripe domains is observed to increase with a corresponding decrease in domain density.

The spin texture during the ZFH experiment shows the reverse temperature-dependent behavior. The LTEM contrast of the stripe domains appears when the temperature increases to 162 K (Figures 4(b)). Interestingly, when the stripe domains are seen to nucleate at the low temperature, their width is small, and the domain walls are wavy. As the temperature is increased to 195 K, the width of the stripe domains greatly increases and the domain walls become smoother. The increased width of domains observed during heating at 250 K is very close to the one observed during cooling at 250 K, which shows that the domain growth and shrinking is a reversible process without any hysteresis. When the temperature reaches 280 K, the stripe domain width again decreases and the density increases. The LTEM contrast finally disappears at 290 K. These results agree with the change in the component of magnetization along the *c*-axis as a function of temperature (Figure 1(a)). Below the paramagnetic-FM transition temperature, the magnetization component along the c-axis increases with decreasing temperature, resulting in the initial domains that are nucleated being small and gradually increasing in size to decrease the domain wall energy, which is dependent on M_s. Similarly while heating, the initial domains that are formed are small and they grow in the size eventually again becoming smaller before disappearing 290 K.

One possibility in region III is that a spin reorientation may occur, which changes the magnetic moment orientation from the c-axis to the *ab* plane. To explore this possibility, we imaged magnetic domains in a TEM lamella fabricated with the c-axis in the plane of the TEM sample (Supporting Figure S5). In this orientation, due to the strong magnetocrystalline anisotropy of $Mn_{1.15}Zn_{0.85}Sb$, we observe the magnetization to be in the plane of the lamella oriented along the c-axis. As the temperature was decreased to below 180 K, we did not observe any changes in the magnetization orientation, which suggests that there is no evident spin reorientation from along the *c* axis to the *ab* plane, or the reoriented net magnetic moment at the temperature Region III is too weak to be measured.

2.4 | Origin of effective DMI

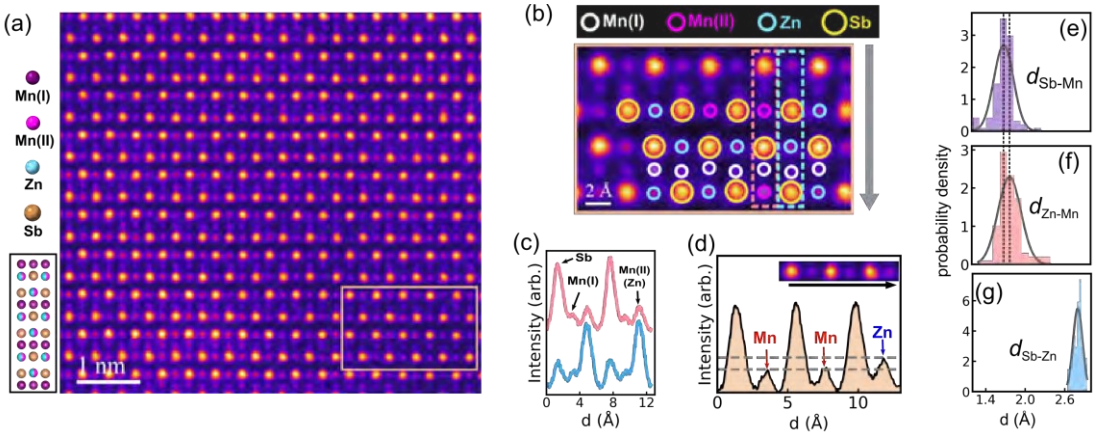

FIGURE 5 Origin of interfiacial DMI. (a) STEM HAADF image showing atomic-resolution crystal structure viewed along the [010] zone axis. The left schematic shows the atomic positions viewed [36] along the [010] zone axis. (b) The spatial distributions of Mn(I) (white circles), Mn(II) (magenta circles), Zn (blue circles) and Sb (yellow circles) atoms in the magnified region that is highlighted by the box in (a). The Mn(I) atoms prefer being located close to Sb atoms. (c) The average intensity of line profiles for two vertical columns, which are labeled by the pink and blue dash box, showing the peaks of Mn(I) sits close to Sb and is away from Zn/(Mn(II)). The gray arrow in (b) indicating the direction of vertical line profile. (d) The average intensity profile along the horizontal direction, for the STEM HAADF image shown in inset and the black arrow the direction of the line profile. The Mn(II) and Zn atoms can be identified by the intensity difference, Mn(II) with lower atomic number having lower-intensity peaks as compared to Zn having higher intensity. The two gray dashed lines indicates the maxima of Mn(II) and Zn peak intensity. (e-g) Histogram of (a) Sb-Mn(I) distance (d_{Sb-Mn}), Zn-Mn(I) distance (d_{Zn-Mn}) and Sb-Zn distance (d_{Sb-Zn}), where the black curve is the normal distribution. The two black dash lines in (e) and (f) highlights the average distance of d_{Sb-Mn} and d_{Zn-Mn}.

In order to elucidate the origins of the DMI that results in the Néel-type spin textures, we performed atomic resolution STEM HAADF imaging to determine atomic positions. The STEM HAADF image seen in Figure 5(a) displays the atomic-resolution structure of the $Mn_{1.15}Zn_{0.85}Sb$ sample viewed along the [010] zone axis. The Mn(I), Zn/Mn(II), and Sb atomic column positions agree very well with the reference crystal structure shown in the left schematic of Figure 5(a)[36]. It should be noted here that Zn is known to replace the Mn atoms at the Mn(II) atomic sites in the crystal structure, as discussed earlier in this paper, however, it not known whether they form an ordered or a disordered structure. Surprisingly, the Mn(I) atoms are not aligned in a straight line, but form a zig-zag trajectory (the white circles in Figure 5(b)). It can

be seen that the Mn(I) sites are preferentially located close to the Sb ions than to the Zn/Mn(II) sites, as shown in Figure 5(b) and from the average intensity profiles shown in Figure 5(c). We statistically evaluated the interatomic distances between the Sb and Mn(I) positions (d_{Sb-Mn}), the Zn/Mn(II) and Mn(I) positions (d_{Zn-Mn}) and the Zn and Sb positions (d_{Sb-Zn}) as shown in the histograms in Figures 5(e−g). The average values of the three projected distances are: $d_{Sb-Mn} = 1.68(\pm 0.15)$ Å, $d_{Zn-Mn} = 1.77(\pm 0.17)$ Å and $d_{Sb-Zn} = 2.80(\pm 0.07)$ Å. The quantitative analysis further illustrates that the Mn(I) ions prefer sitting further away from Zn/Mn(II) sites and closer to the Sb ions. The physical mechanism to form this local structure defect may be complicated, which involves electrostatic interaction and magnetic correlation from neighboring ions, as well as atom size, during the growth of crystal. For example, this might attribute to electrostatic interaction between $Mn(I)^{+1}$ and Sb^{-3} is attractive and stronger compared to that between $Mn(I)^{+1}$ and Zn^{+2} ($M(II)^{+2}$) which is repulsive[37]. In addition, we observe that the Mn(II) substitution by Zn is not uniform or ordered across the sample. Although Mn(II) and Zn ions have very close atomic number of $Z = 25$ and $Z = 30$, respectively, thereby making it difficult to determine them in a HAADF image based on intensity, we did careful measurements of the intensity line profiles of several atomic columns as shown in Figure 5(d). Based on these measurements, we are able to see that Zn substitution on the Mn(II) sites occurs randomly across the crystal. Therefore, the displacement of Mn(I) ions results in a local symmetry breaking, which induces effective DMI. The local defects have been reported to enhance the DMI[50]. The similar phenomenon was also reported by C. Liu et al.[51], the so-called effective DMI giving rise to Néel skyrmion.

3 | DISCUSSION AND CONCLUSIONS

Zn-rich $Mn_{1.15}Zn_{0.85}Sb$ exhibits two magnetic phase transitions that are related to temperature. The magnetic properties, such as teh magnetic anisotropy, coercive field and remnant magnetization, are also highly dependent on temperature, leading to clear changes in spin texture in the three temperature regimes. The temperature-dependent magnetic behavior is due to the changes in the magnetic interactions between the two Mn sublattices thereby affecting the FiM order. The transition from paramagnetic to FiM order occurs at first transition temperature. Due to the significantly high magnetization, this state is effectively a weak FiM state. At the second transition temperature the phase transition is from a FiM state to a stronger FiM state. It has been reported that out-of-plane spins at the Mn(I) and Mn(II) sites reorient to the in-plane direction in Mn_2Sb across the second phase transition temperature, resulting in the decrease in the magnetization along the *c* axis[30]. However, we do not see obvious switching from an out-of-plane magnetization to an in-plane magnetization in thin or bulk crystals at the low-temperature Region III, using either LTEM or MOKE imaging. We also performed temperature-dependent X-ray diffraction, which did not show any changes in the crystal structure, therefore eliminating the possibility of a magneto-structural transition (see the Supporting Figure S6). Thus, the changes in magnetic phase are due to changes in the magnetic interactions as a function of temperature in the Zn-doped $Mn_{2-x}Zn_xSb$ system.

We can further understand the formation of skyrmions in this material based on the critical material parameter for the skyrmion stability[52], $\kappa = \pi D / 4\sqrt{AK_u}$, where D is the DMI coefficient, A is the micromagnetic exchange constant, and K_u is the uniaxial anisotropy constant. As the temperature changes from region I to region III, the effective anisotropy of $Mn_{1.15}Zn_{0.85}Sb$ gradually increases as determined from the change in the coercive field and the remnant magnetization. This increase in anisotropy is inversely proportional to κ and hence reduces the tendency of the material to form stable skyrmions. A similar observation was also made for

FiM multilayers of [Pt/$Fe_{1-x}Tb_x$/Ta] [27].

In summary, we have explored the temperature-dependent magnetic properties of $Mn_{1.15}Zn_{0.85}Sb$, and have confirmed the presence of non-trivial chiral Néel spin textures in the thin lamella via direct visualization. The resulting spin textures show very different behavior in three distinct temperature regions. The unique skyrmion bag spin textures are formed only in the presence of a strong perpendicular anisotropy (Region II). The displacement of the Mn(I) atomic sites toward the Sb sites results in an effective DMI that enables the formation of the Néel-type spin textures. Our work thus demonstrates interesting pathways to introduce a symmetry-breaking DMI interaction in centrosymmetric crystal structures through doping. Our study shows the existence of rich topological spin textures in FiMs, which can be controlled by temperature and magnetic fields, thereby making this material a promising candidate for future applications in spintronics or information storage.

Methods

Crystal Synthesis: Single crystals of $Mn_{2-x}Zn_xSb$ were grown with a self-flux method using a Zn flux. To initiate the growth process of an $Mn_{1.15}Zn_{0.85}Sb$ crystal, Mn powder (99.6%, Alpha Aesar), Zn powder (99.9%, Alpha Aesar), and Sb powder (99.5%, Beantown Chemical) were loaded in an alumina crucible at a atomic ratio of Mn : Zn : Sb = 1.2 *:* 6 : 1. The crucible was then sealed in a quartz tube evacuated below 10^{-1} Pa. The tube was gradually heated over 30 –40 h to reach the maximum temperature of 900 °C, held at this temperature for 3 days, slowly cooled down (3 K /min) to 600 °C, followed by subsequent centrifuge to remove the Zn flux.

Magnetization characterization: The temperature-dependent magnetization was measured using a superconducting quantum interference device (SQUID) magnetometer. The crystal was cooled down from 330 K to 2 K without (with) an applied magnetic field for the ZFC (FC) run,

with the field applied along the *c* axis of the $Mn_{1.15}Zn_{0.85}Sb$ crystal. The strength of the magnetic moment was recorded with a 50 mT or 100 mT magnetic field applied when heating the sample from 2 K to 330 K. The calculated density of the $Mn_{1.15}Zn_{0.85}Sb$ crystal (7.33 gcm^{-3}) was used to normalize the magnetization to mass.

The field-dependent magnetization was measured using a physical properties measurement system (PPMS). The sample was mounted in a standard quartz holder for in-plane magnetization measurements, while a standard brass holder was used for out-of-plane magnetization measurements. Isothermal magnetization measurements were performed by sweeping the applied magnetic field between -9 T and 9 T for hysteresis loop measurements. To ensure accurate magnetization measurements, the background signal from the sample holder was separately measured and subtracted.

MOKE measurement: Polar-MOKE images were recorded using a commercial microscope from Evico magnetics. The bulk $Mn_{1.15}Zn_{0.85}Sb$ sample was mounted using GE varnish inside an optical cryosta,t which was cooled using liquid nitrogen to obtain a minimum temperature of 80 K. An in-house made solenoid was utilized to apply magnetic fields up to 135 mT, perpendicular to the crystal surface being imaged. Magnetic contrast was optimized by subtracting a MOKE image taken at a saturating field of 135 mT from images acquired at lower fields. However, magnetic domains of the $Mn_{1.15}Zn_{0.85}Sb$ crystal cannot be polarized by a 135 mT magnetic field when the temperature is 120 K. Therefore, the magnetic contrast cannot be improved and contaminating black spots cannot be removed using this approach.

TEM experiment: Thin $Mn_{1.15}Zn_{0.85}Sb$ lamellae for TEM analysis were prepared using a Zeiss NVision focused ion beam (FIB) system. The cryo LTEM measurements were carried out using a Gatan liquid nitrogen holder. The experiment to confirm the Néel-type domains was carried out using a FEI Tecnai F20ST TEM operating in Lorentz mode at 200 kV. The LTEM images as a function of temperature were recorded on a JEOL 2100F TEM with an image corrector. The STEM HAADF experiment to analyse atomic-resolution structure was carried

out in a ThermoFisher Scientific Spectra 200 with the 200 kV accelerating voltage.

Supporting Information

Supporting Information is available from the Wiley Online Library or from the author.

Acknowledgements

Work at Argonne National Laboratory was funded by the US Department of Energy, Office of Science, Office of Basic Energy Sciences, Materials Science and Engineering Division. Use of the Center for Nanoscale Materials, an Office of Science user facility, was supported by the U.S. Department of Energy, Office of Science, Office of Basic Energy Sciences, under Contract No. DE-AC02-06CH11357. J.H. acknowledges support from the National Science Foundation under Grant No. DMR-2238254

Conflict of Interest

The authors declare no conflict of interest.

Data Availability Statement

The data that support the findings of this study are available from the corresponding author upon reasonable request.

References

[1] N. Nagaosa, Y. Tokura, *Nat. Nanotechnol.* **2013**, *8*, 12 899.

[2] A. Fert, N. Reyren, V. Cros, *Nat. Rev. Mater.* **2017**, *2*, 7 1.

[3] A. N. Bogdanov, C. Panagopoulos, *Nat. Rev. Phys.* **2020**, *2*, 9 492.

[4] C. Back, V. Cros, H. Ebert, K. Everschor-Sitte, A. Fert, M. Garst, T. Ma, S. Mankovsky, T. L. Monchesky, M. Mostovoy, N. Nagaosa, S. S. P. Parkin, C. Pfleiderer, N. Reyren, A. Rosch, Y. Taguchi, Y. Tokura, K. von Bergmann, J. Zang **2019**.

[5] S. Mühlbauer, B. Binz, F. Jonietz, C. Pfleiderer, A. Rosch, A. Neubauer, R. Georgii, P. Böni, *Science* **2009**, *323*, 5916 915.

[6] X. Z. Yu, N. Kanazawa, Y. Onose, K. Kimoto, W. Z. Zhang, S. Ishiwata, Y. Matsui, Y. Tokura, *Nat. Mater.* **2011**, *10*, 2 106.

[7] Y. Tokunaga, X. Z. Yu, J. S. White, H. M. Rønnow, D. Morikawa, Y. Taguchi, Y. Tokura, *Nat. Commun.* **2015**, *6*, May 7638.

[8] W. Jiang, P. Upadhyaya, W. Zhang, G. Yu, M. B. Jungfleisch, F. Y. Fradin, J. E. Pearson, Y. Tserkovnyak, K. L. Wang, O. Heinonen, S. G. E. te Velthuis, A. Hoffmann, *Science* **2015**, *349*, 6245 283.

[9] S. Woo, K. Litzius, B. Krüger, M.-Y. Im, L. Caretta, K. Richter, M. Mann, A. Krone, R. M. Reeve, M. Weigand, P. Agrawal, I. Lemesh, M.-A. Mawass, P. Fischer, M. Kläui, G. S. D. Beach, *Nat. Mater.* **2016**, *15*, 5 501.

[10] W. Jiang, S. Zhang, X. Wang, C. Phatak, Q. Wang, W. Zhang, M. B. Jungfleisch, J. E. Pearson, Y. Liu, J. Zang, X. Cheng, A. Petford-Long, A. Hoffmann, S. G. E. te Velthuis, *Phys. Rev. B* **2019**, *99*, 10 104402.

[11] H. Zhang, Y. Zhang, Z. Hou, M. Qin, X. Gao, J. Liu, *Mater. Futures.* **2023**, *2*, 3 032201.

[12] G. Finocchio, F. Büttner, R. Tomasello, M. Carpentieri, M. Kläui, *J. Phys. D: Appl. Phys.* **2016**, *49*, 42 423001.

[13] S. K. Kim, G. S. D. Beach, K.-J. Lee, T. Ono, T. Rasing, H. Yang, *Nat. Mater.* **2022**, *21*, 1 24.

[14] Y. Zhang, X. Feng, Z. Zheng, Z. Zhang, K. Lin, X. Sun, G. Wang, J. Wang, J. Wei, P. Vallobra, Y. He, Z. Wang, L. Chen, K. Zhang, Y. Xu, *Appl. Phys. Rev.* **2023**, *10*, 1 011301.

[15] Y. Quessab, J.-W. Xu, C. T. Ma, W. Zhou, G. A. Riley, J. Shaw, H. Nembach, S. Poon, A. D. Kent, *Sci. Rep.* **2020**, *10*, 1 7447.

[16] S. Ding, A. Ross, R. Lebrun, S. Becker, K. Lee, I. Boventer, S. Das, Y. Kurokawa, S. Gupta, J. Yang, G. Jakob, M. Kläui, *Phys. Rev. B* **2019**, *100* 100406.

[17] D.-H. Kim, M. Haruta, H.-W. Ko, G. Go, H.-J. Park, T. Nishimura, D.-Y. Kim, T. Okuno, Y. Hirata, Y. Futakawa, H. Yoshikawa, W. Ham, S. Kim, H. Kurata, A. Tsukamoto, Y. Shiota, T. Moriyama, S.-B. Choe, K.-J. Lee, T. Ono, *Nat. Mater.* **2019**, *18*, 7 685.

[18] W. Jiang, X. Zhang, G. Yu, W. Zhang, X. Wang, M. Benjamin Jungfleisch, J. E. Pearson, X. Cheng, O. Heinonen, K. L. Wang, Y. Zhou, A. Hoffmann, S. G. E. te Velthuis, *Nat. Phys.* **2017**, *13*, 2 162.

[19] K. Litzius, I. Lemesh, B. Krüger, P. Bassirian, L. Caretta, K. Richter, F. Büttner, K. Sato, O. A. Tretiakov, J. Förster, R. M. Reeve, M. Weigand, I. Bykova, H. Stoll, G. Schütz, G. S. D. Beach, M. Kläui, *Nat. Phys.* **2017**, *13*, 2 170.

[20] X. Zhang, Y. Zhou, M. Ezawa, *Nat. Commun.* **2016**, *7* 10293.

[21] S. Woo, K. M. Song, X. Zhang, Y. Zhou, M. Ezawa, X. Liu, S. Finizio, J. Raabe, N. J. Lee, S.-I. Kim, S.-Y. Park, Y. Kim, J.-Y. Kim, D. Lee, O. Lee, J. W. Choi, B.-C. Min, H. C. Koo, J. Chang, *Nat. Commun.* **2018**, *9*, 1 959.

[22] D.-H. Kim, M. Haruta, H.-W. Ko, G. Go, H.-J. Park, T. Nishimura, D.-Y. Kim, T. Okuno, Y. Hirata, Y. Futakawa, H. Yoshikawa, W. Ham, S. Kim, H. Kurata, A. Tsukamoto, Y. Shiota, T. Moriyama, S.-B. Choe, K.-J. Lee, T. Ono, *Nat. Mater.* **2019**, *18*, 7 685.

[23] J. Brandão, D. A. Dugato, M. V. Puydinger dos Santos, J. C. Cezar, *ACS Appl. Nano Mater.* **2019**, *2*, 12 7532, publisher: American Chemical Society.

[24] H. Wu, F. Groß, B. Dai, D. Lujan, S. A. Razavi, P. Zhang, Y. Liu, K. Sobotkiewich, J. Förster, M. Weigand, G. Schütz, X. Li, J. Gräfe, K. L. Wang, *Adv. Mater.* **2020**, *32*, 34 2003380.

[25] K. Chen, D. Lott, A. Philippi-Kobs, M. Weigand, C. Luo, F. Radu, *Nanoscale* **2020**, *12*, 35 18137.

[26] X. Wang, A. R. Stuart, M. S. Swyt, C. M. Q. Flores, A. T. Clark, A. Fiagbenu, R. V. Chopdekar, P. N. Lapa, Z. Xiao, D. Keavney, R. Rosenberg, M. Vogel, J. E. Pearson, S. G. E. t. Velthuis, A. Hoffmann, K. S. Buchanan, X. M. Cheng, *Phys. Rev. Mater.* **2022**, *6*, 8 084412.

[27] T. Xu, Y. Zhang, Z. Wang, H. Bai, C. Song, J. Liu, Y. Zhou, S.-G. Je, A. T. N'Diaye, M.-Y. Im, R. Yu, Z. Chen, W. Jiang, *ACS Nano* **2023**, *17*, 8 7920.

[28] C. Luo, K. Chen, V. Ukleev, S. Wintz, M. Weigand, R.-M. Abrudan, K. Prokeš, F. Radu, *Commun. Phys.* **2023**, *6*, 1 1.

[29] R. Streubel, C.-H. Lambert, N. Kent, P. Ercius, A. T. N'Diaye, C. Ophus, S. Salahuddin, P. Fischer, *Adv. Mater.* **2018**, *30*, 27 1800199.

[30] M. K. Wilkinson, N. S. Gingrich, C. G. Shull, *J. Phys. Chem. Solids* **1957**, *2*, 4 289.

[31] L. Heaton, N. S. Gingrich, *Acta Crystallogr.* **1955**, *8*, 4 207.

[32] M. R. U. Nabi, R. Basnet, K. Pandey, S. K. Chhetri, D. Upreti, G. Acharya, F. Wang, A. Fereidouni, H. O. Churchill, Y. Guan, G. Yingdong, H. Jin, *Acta Mater.* **2023**, *259* 119251.

[33] J. S. Wilden, A. Hoser, M. Chikovani, J. Perßon, J. Voigt, K. Friese, A. Grzechnik, *Inorganics* **2018**, *6*, 4 113.

[34] J. Goto, T. Kakimoto, S. Fujii, K. Koyama, *Mater. Trans.* **2013**, *54*, 12 2309.

[35] A. Austin, E. Adelson, W. Cloud, *Phys. Rev.* **1963**, *131*, 4 1511.

[36] M. R. U. Nabi, A. Wegner, F. Wang, Y. Zhu, Y. Guan, A. Fereidouni, K. Pandey, R. Basnet, G. Acharya, H. O. Churchill, G. Yingdong, H. Jin, *Phys. Rev. B* **2021**, *104*, 17 174419.

[37] V. Johnson, W. Jeitschko, *J. Solid State Chem.* **1977**, *22*, 1 71.

[38] V. M. Ryzhkovskii, V. I. Mitsiuk, *Inorg. Mater.* **2010**, *46* 581.

[39] P. A. E. Murgatroyd, K. Routledge, S. Durdy, M. W. Gaultois, T. W. Surta, M. S. Dyer, J. B. Claridge, S. N. Savvin, D. Pelloquin, S. Hébert, J. Alaria, *Adv. Funct. Mater.* **2021**, *31*, 17 2100108.

[40] D. Foster, C. Kind, P. J. Ackerman, J.-S. B. Tai, M. R. Dennis, I. I. Smalyukh, *Nat. Phys.* **2019**, *15*, 7 655.

[41] J. Tang, Y. Wu, W. Wang, L. Kong, B. Lv, W. Wei, J. Zang, M. Tian, H. Du, *Nat. Nanotechnol.* **2021**, *16*, 10 1086.

[42] M. R. U. Nabi, Y. Li, S. G. E. te Velthuis, S. K. Chhetri, D. Upreti, R. Basnet, G. Acharya, C. Phatak, J. Hu, *Adv. Phys. Res.* **2024**, 2300145.

[43] J. Brandão, D. A. Dugato, M. V. P. dos Santos, F. Béron, J. C. Cezar, *Appl. Surf. Sci.* **2022**, *585* 152598.

[44] W. Szmaja, J. Grobelny, M. Cichomski, *Czech. J. Phys.* **2004**, *54*, Suppl 4 249.

[45] M. Benitez, A. Hrabec, A. Mihai, T. Moore, G. Burnell, D. McGrouther, C. Marrows, S. McVitie, *Nat. Commun.* **2015**, *6*, 1 8957.

[46] S. Jin, Y. Wang, H. Zheng, S. Dong, K. Han, Z. Wang, G. Wang, X. Jiang, X. Wang, J. Hong, H. Huang, Y. Zhang, T.-L. Xia, X. Wang, *Nano Lett.* **2024**, *24*, 18 5467.

[47] A. K. Gopi, A. K. Srivastava, A. K. Sharma, A. Chakraborty, S. Das, H. Deniz, A. Ernst, B. K. Hazra, H. L. Meyerheim, S. S. P. Parkin, *ACS nano* **2024**, *18*, 7 5335.

[48] S. Middelhoek, *J. Appl. Phys.* **1963**, *34*, 4 1054.

[49] S. Grebenchuk, C. McKeever, M. Grzeszczyk, Z. Chen, M. Šiškins, A. R. McCray, Y. Li, A. K. Petford-Long, C. M. Phatak, D. Ruihuan, L. Zheng, K. S. Novoselov, E. J. G. Santos, M. Koperski, *Adv. Mater.* **2024**, *36* 2311949.

[50] P. C. Carvalho, I. P. Miranda, J. Brandão, A. Bergman, J. C. Cezar, A. B. Klautau, H. M. Petrilli, *Nano Lett.* **2023**, *23*, 11 4854.

[51] C. Liu, J. Jiang, C. Zhang, Q. Wang, H. Zhang, D. Zheng, Y. Li, Y. Ma, H. Algaidi, X. Gao, Z. Hou, W. Mi, J. Liu, Z. Qiu, X. Zhang, *Adv. Sci.* **2023**, *10*, 27 2303443.

[52] A. Soumyanarayanan, M. Raju, A. L. Gonzalez Oyarce, A. K. C. Tan, M.-Y. Im, A. P. Petrović, P. Ho, K. H. Khoo, M. Tran, C. K. Gan, F. Ernult, C. Panagopoulos, *Nat. Mater.* **2017**, *16*, 9 898.